

Scale Recovery for Monocular Visual Odometry Using Depth Estimated with Deep Convolutional Neural Fields

Xiaochuan Yin*, Xiangwei Wang*, Xiaoguo Du, Qijun Chen
Tongji University

yinxiaochuan@hotmail.com, wangxiangwei.cpp@gmail.com, {1610448, qjchen}@tongji.edu.cn

Abstract

Scale recovery is one of the central problems for monocular visual odometry. Normally, road plane and camera height are specified as reference to recover the scale. The performances of these methods depend on the plane recognition and height measurement of camera. In this work, we propose a novel method to recover the scale by incorporating the depths estimated from images using deep convolutional neural fields. Our method considers the whole environmental structure as reference rather than a specified plane. The accuracy of depth estimation contributes to the scale recovery. We improve the performance of depth estimation by considering two consecutive frames and egomotion of camera into our networks. The depth refinement and scale recovery are obtained iteratively. In this way, our method can eliminate the scale drift and improve the depth estimation simultaneously. The effectiveness of our method is verified on the KITTI dataset for both monocular visual odometry and depth estimation tasks.

1. Introduction

Visual odometry is the process of estimating the egomotion of the robot from input images. It is one of the core modules of simultaneous localization and mapping (SLAM) system. Visual odometry using stereo camera has achieved a great success these years. The reason why stereo visual odometry is widely applied is that it can estimate a reliable depth map for transformation matrix calculation. However, stereo camera will degenerate into a monocular one when the distance between camera and scene is much larger than the baseline. Moreover, self-calibration is also required for stereo visual odometry system after long-term operation in order to reduce the mechanical vibration encountered in application [5, 23]. Unlike the stereo visual odometry, visual odometry using monocular camera does not suffer from these problems. Therefore, monocular visual odometry has



Figure 1. 3D reconstruction of street scene with egomotion and depth estimated by our method.

attracted a lot of attentions in recent years.

Monocular visual odometry algorithms cannot get environment map and robot motion in real scale. Because the distance between features and camera cannot be measured by triangulation directly. Therefore, monocular visual odometry faces the problem of scale drift, and the absolute scale need to be recovered to eliminate it.

To recover the scale, geometry constraints between the camera and the surroundings are normally used. Previous methods apply the camera height and the ground surface to obtain the scale [2, 24, 15]. The camera height is assumed to be known in advance. In [2], they adopt a texture analysis classifier to extract the ground region, and in this way the planar homography matrix is calculated to recover the scale factor. In [24], a combination of several cues within a predefined region of interest (ROI) is used to recover the scale. To be more robust in different scenes, [15] estimates the ground geometry with self-learned ground appearance information. These methods are constrained by limited environmental information. More structural information of environments is required. In this way, there would not need to set the camera height and ground plane as the fixed references.

In these years, deep learning has achieved a great success

* Authors contributed equally

in the computer vision field for its powerful feature learning ability. Deep learning may promote the progress of visual odometry [1]. In [4], estimator based on deep convolutional neural networks is trained for egomotion estimation from optical flow. Depth estimation of surroundings would be another plausible direction for this problem. Depth estimation from single image is a challenging task. Depth estimation and scene structure inference with Markov Random Field (MRF) is proposed in [22]. In [6, 7], a novel pixel-wise depth and surface normal regression neural networks are proposed. Depth can also be refined via hierarchical conditional random fields (CRFs) after regression from deep convolutional networks [17]. In [18], deep convolutional neural networks combined with condition random fields (convolutional neural fields) are applied to estimate depth from picture taken in indoor and outdoor environments. For consecutive frames, optical flow is applied to extract depth information [12, 21].

In this paper, we introduce a novel scale recovery method using depth estimated from images with deep neural networks. We calculate the scale of translation from the estimated depth map. The depth prediction is improved by considering consecutive images and motion constraints into our method. Therefore, convolutional neural fields are used for depth estimation in our system, which concatenate convolutional neural networks and conditional random fields. The convolutional neural networks can regress a coarse depth map from input images. Then the conditional random fields refine the coarse depth by involving the constraints. The scale of egomotion is obtained based on the refined depth. In this way, the depth and scale can be calculated iteratively. The contributions of our paper are as follows.

1. We present a novel scale recovery method for monocular visual odometry.
2. We present novel neural networks for depth estimation from images. It takes consecutive frames and motion constraints into consideration to improve the result.
3. Our method can alleviate the scale drift problem caused by the accumulated error.
4. A novel monocular visual odometry system is proposed using deep learning.

The structure of this paper is organized as follows. In section II, we introduce the background knowledge of the relationship between photo intensity and camera motion. The neural networks for depth estimation with consecutive pictures and egomotion are proposed in section III. In section IV, we introduce our scale calculation method and framework of our system. Experiments are conducted and analyzed in section V. We conclude our paper in the last section.

2. Background

In this section, we introduce the background knowledge of our system. In this paper, bold capital letters denote a matrix, bold lower-case letters a column vector, others a scalar. The intensity of pixel $\mathbf{u} = (u, v)^T \in \Omega$ in the image is $I : \Omega \subset \mathbb{R}^2 \mapsto \mathbb{R}$. The 3D point in the world coordinate $\mathbf{p} = (x, y, z)^T \in \mathbb{R}^3$ of the pixel \mathbf{u} can be obtained from the inverse projection function $\pi : \mathbb{R}^2 \mapsto \mathbb{R}^3$.

$$\mathbf{p} = \pi^{-1}(\mathbf{u}, z_{\mathbf{u}}) = z_{\mathbf{u}} \left(\frac{u - c_x}{f_x}, \frac{v - c_y}{f_y}, 1 \right)^T \quad (1)$$

where $z_{\mathbf{u}}$ is the depth of pixel \mathbf{u} , f_x, f_y and c_x, c_y denotes the focal length and optical center in the standard pinhole camera model, respectively.

The rotation matrix $\mathbf{R} \in SO(3)$ and translation vector $\mathbf{t} \in \mathbb{R}^3$ can transform the point \mathbf{p} to the new position.

$$\mathcal{T}(\mathbf{T}, \mathbf{p}) = \mathbf{R}\mathbf{p} + \mathbf{t} \quad (2)$$

The residual of the i -th pixel is defined as the difference in intensity between the first and second image. In this work, the intensity of pixels after reprojection is assumed to be the same.

$$r_{i,I} := I_2 \left(\pi \left(\mathcal{T} \left(\mathbf{T}, \pi^{-1}(\mathbf{u}_{1,i}, z_{1,\mathbf{u}_i}) \right) \right) \right) - I_1(\mathbf{u}_{1,i}) \quad (3)$$

$$\overline{\mathcal{R}} = \{ \mathbf{u} | \mathbf{u} \in \overline{\mathcal{R}}_{k-1} \wedge \pi \left(\mathcal{T}(\mathbf{T}, \pi^{-1}(\mathbf{u}, z_{\mathbf{u}})) \right) \in \Omega_k \} \quad (4)$$

where π is the projection function which is defined as:

$$\mathbf{u} = \pi(\mathbf{p}) = \left(\frac{f_x x}{z} + c_x, \frac{f_y y}{z} + c_y \right).$$

3. Depth Estimation with Convolutional Neural Fields

In this section, we will introduce the structure of our deep neural networks for depth estimation. In order to increase the accuracy of depth prediction and remove the outliers, two consecutive images and the egomotion are taken as inputs in our networks. We construct our convolutional neural fields by concatenating the convolutional neural networks and conditional random fields.

We apply the deep residual neural networks (ResNet) [10] and fully convolutional networks [19] to construct the convolutional part of our networks. ResNet is an elegant structure, and it has achieved excellent performances [10]. It takes standard convolutional neural networks and adds skip connections that bypass a few convolutional layers to construct the residual block. ResNet has a powerful ability for feature representation. However, convolutional and pooling layers would generate the downsampling features.

For the scale recovery problem, we need the depth values of whole image. We apply the fully convolutional networks to upsampling the regressed depth map to the input's size. In order to refine the depth map for later use, we apply the conditional random fields to smooth the regressed result. The structure of our neural networks is shown in Figure 2. The detail of this part can refer to their elegant work in [10] [19]. Next, we will present our conditional random fields part for depth refinement.

3.1. Refining the regression results via CRFs

Depth can be predicted using convolutional part mentioned above. However, output of the above networks has outliers and may introduce additional errors for the scale recovery process. Therefore, additional layer is required to refine the generated depth. Conditional random fields are commonly used to involve constraints to improve the results. In this work, we define an energy function as follows.

$$E = \sum_{\mathbf{p} \in \Omega_1} U(y_{1,\mathbf{p}}, x_{1,\mathbf{p}}) + \omega_1 \sum_{(\mathbf{p}, \mathbf{q}) \in \Omega_1} V(y_{1,\mathbf{p}}, y_{1,\mathbf{q}}, x_{1,\mathbf{p}}, x_{1,\mathbf{q}}) + \omega_2 \sum_{(\mathbf{p}, \mathbf{q}) \in \bar{\mathcal{R}}} W(x_{1,\mathbf{p}}, y_{1,\mathbf{p}}, x_{2,\mathbf{q}}, \mathbf{T}) \quad (5)$$

where $x_{i,\mathbf{p}}$ denotes the pixel \mathbf{p} in image Ω_i . $y_{i,\mathbf{p}}$ is the depth of pixel \mathbf{p} in image Ω_i . \mathbf{T} is the transformation matrix of robot. ω_1 and ω_2 are coefficients of last two terms. They reflect the influences of each part, and they are obtained in our training process. Our energy function consists of three potential functions: unary potential, pairwise potential in the same image and pairwise potential of two consecutive images.

3.1.1 Unary potential

The unary potential function measures the least square loss between the regressed depth z and ground truth depth y . The regressed depth z is the output of the convolutional part and it is taken as input to the conditional random fields for refinement. The unary potential part is defined as:

$$U(y_{1,\mathbf{p}}, x_{1,\mathbf{p}}; \theta) = \frac{1}{2}(y_{1,\mathbf{p}} - z_{1,\mathbf{p}}(x_{1,\mathbf{p}}; \theta))^2, \quad \forall \mathbf{p} \in \Omega_1 \quad (6)$$

where θ are the parameters of the convolutional part of our networks.

3.1.2 Pairwise potential in the same image

The pairwise potential term enforces the coherent of neighboring pixel's depth. We assume that the neighboring pixels

with similar color are close in depth.

$$V(y_{\mathbf{p}}, y_{\mathbf{q}}, x_{\mathbf{p}}, x_{\mathbf{q}}; \gamma_1, \gamma_2) = \frac{1}{2} \mathbf{R}_{\mathbf{p}\mathbf{q}} (y_{\mathbf{p}} - y_{\mathbf{q}})^2, \quad \forall \mathbf{p}, \mathbf{q} \in \Omega_1 \quad (7)$$

where $\mathbf{R}_{\mathbf{p},\mathbf{q}}$ is the appearance kernel, which is used to measure the distance and color between different pixels.

$$\mathbf{R}_{\mathbf{p},\mathbf{q}} = \exp(-\gamma_1 \|I_{\mathbf{p}} - I_{\mathbf{q}}\|^2 - \gamma_2 \|\mathbf{u}_{\mathbf{p}} - \mathbf{u}_{\mathbf{q}}\|^2) \quad (8)$$

where $I_{\mathbf{p}}$ and $\mathbf{u}_{\mathbf{p}}$ are the color and position of the pixel \mathbf{p} ; γ_1 and γ_2 denote the importance of each kernel.

3.1.3 Pairwise potential of two consecutive images

In order to consider the constraints between two consecutive images, the third potential function measures accuracy of depth estimation by projecting the current frame to the previous one with known transformation matrix. Because the intensity error r does not follow the Gaussian distribution. Therefore, the Huber loss function is applied in our energy function to eliminate the effects of outliers.

$$W = \frac{1}{2} \|r_i(\mathbf{T}, \mathbf{u}, z) + \mathbf{J}_i(y - z)\|_{Huber} \quad (9)$$

where \mathbf{J}_i is the Jacobian of the r_i at pixel \mathbf{u} with depth point z and transformation matrix \mathbf{T} .

3.2. Training the neural networks

The probability distribution function of depth is

$$Pr(\mathbf{y}|\mathbf{x}) = \frac{1}{Z(\mathbf{x})} \exp(-E(\mathbf{y}, \mathbf{x})) \quad (10)$$

The partition function $Z(\mathbf{x})$ is defined as:

$$Z(\mathbf{x}_1, \mathbf{x}_2, \mathbf{T}) = \int_{\mathbf{y}} \exp\{-E(\mathbf{y}, \mathbf{x}_1, \mathbf{x}_2, \mathbf{T})\} d\mathbf{y}. \quad (11)$$

Because the Huber loss function is applied in our energy function, we cannot obtain the partition function for maximum a posteriori estimation by calculating the integral in the partition function analytically. Therefore, the neural networks are trained through the score matching [11] without requiring normalization. The discrete version of the score matching is adopted to optimize the objective function

$$\mathcal{J}(\delta) = \frac{1}{N} \sum_{i=1}^N \sum_{\delta} \left(\partial \varphi_i(\delta) + \frac{1}{2} \varphi_i(\delta)^2 \right) + const \quad (12)$$

where $\delta = [\mathbf{z}(\theta)^T, \omega_1, \omega_2]^T$ are the parameters to optimize in conditional random fields. The score function is defined as:

$$\varphi(\mathbf{y}; \delta) = \nabla_{\mathbf{y}} \log Pr(\mathbf{y}|\delta) \quad (13)$$

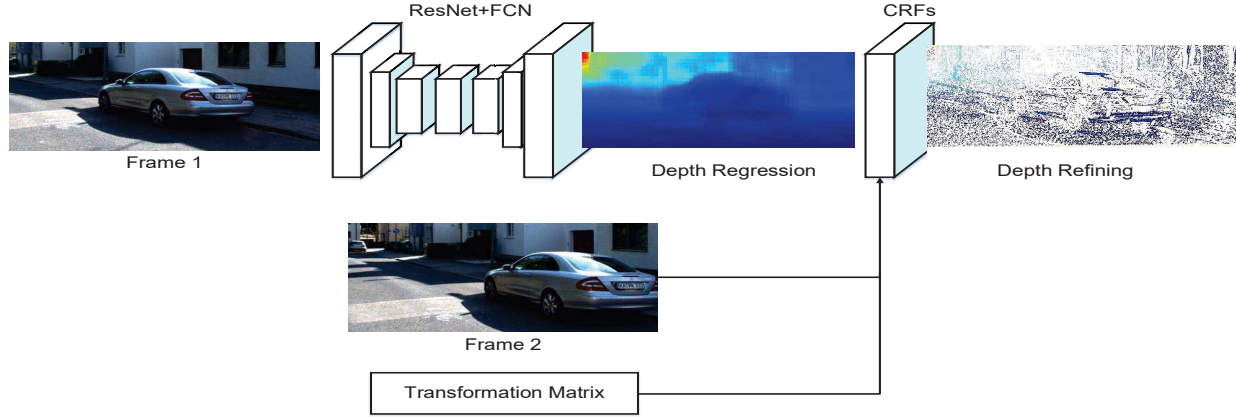


Figure 2. Structure of our neural networks. The inputs of neural networks are two consecutive frames and transformation matrix. Output is the refined depth map. The deep convolutional part is composed of deep residual networks and fully convolutional networks. The output of the convolutional part is refined by the following conditional random fields layer.

The i -th element of the model score function with respect to the i -th variable is

$$\partial_i \varphi_i(\mathbf{y}; \delta) = \frac{\partial \varphi_i(\mathbf{y}; \delta)}{\partial y_i} \quad (14)$$

The variable δ can be optimized with gradient descent

$$\delta \leftarrow \delta - \eta \frac{\partial \mathcal{J}}{\partial \delta}. \quad (15)$$

The parameters of our convolutional neural fields $\{\theta, \omega_1, \omega_2\}$ can be obtained by backpropagation.

3.3. Depth estimation

The refined depth can be calculated by solving the MAP inference

$$\mathbf{y} = \underset{\mathbf{y}}{\operatorname{argmax}} \log Pr(\mathbf{y} | \mathbf{x}_1, \mathbf{x}_2, \mathbf{T}). \quad (16)$$

In the depth estimation process, the Huber loss function is replaced with mean squared loss if the intensity error of pixels in two consecutive frames is smaller than a given threshold, otherwise the depth value is removed.

The negative log-likelihood can be written as:

$$-\log Pr(\mathbf{y} | \mathbf{x}_1, \mathbf{x}_2, \mathbf{T}) = \frac{1}{\hat{N}} (\|\mathbf{y} - \mathbf{z}\|^2 + \omega_1 \mathbf{y}^T \mathbf{M} \mathbf{y} + \omega_2 \|\mathbf{r} + \mathbf{J}(\mathbf{y} - \mathbf{z})\|^2) \quad (17)$$

where \hat{N} is the number of inliers; $\mathbf{M} = \mathbf{D} - \mathbf{R}$ is the graph Laplacian matrix; \mathbf{R} is the affinity matrix composed of R_{pq} ; \mathbf{D} is the diagonal matrix with $D_{pp} = \sum_q R_{pq}$; \mathbf{J} is the Jacobian matrix of the image with respect of the depth, and \mathbf{J} is the diagonal matrix with $\mathbf{J}_{pp} = J_p$.

The refined depth can be calculated as:

$$\mathbf{y} = (\mathbf{I} + \omega_1 \mathbf{M} + \omega_2 \mathbf{J}^2)^{-1} (\mathbf{z} + \omega_2 \mathbf{J}^2 \mathbf{z} - \omega_2 \mathbf{J} \mathbf{r}) \quad (18)$$

The training process of our neural networks is shown in Algorithm 1. We train the neural networks with mean squared loss as criteria at first. Then the CRFs layer is added and we train the whole networks. The errors and gradients are set to zeros for the pixel without ground truth depth.

Algorithm 1: Training process of convolutional neural fields

Input: Given the input image sequence $\{\mathbf{X}_i\}_{i=1}^N$, $\mathbf{X}_i \in \mathbb{R}^{3 \times m \times n}$, the corresponding output depth maps $\{\mathbf{Y}_i\}_{i=1}^N$, $\mathbf{Y}_i \in \mathbb{R}^{m \times n}$ and the transformation matrix $\{\mathbf{T}_i\}_{i=1}^N$

Initialize: ResNet is obtained from model zoo.

Output: Parameters of networks θ , ω_1 and ω_2

// Pre-training the ResNet+FCN with mean squared loss

// Training the networks include the CRFs layer

for $t = 1$ to \maxIteration **do**

 Randomly select input \mathbf{X}_i^t , \mathbf{X}_i^{t+1} and \mathbf{T}

 // Forward propagation

 Obtain refined depth map $\hat{\mathbf{Y}}_i$

 Obtain the gradient from Eq. (15)

 // Backpropagation

 Update θ , ω_1 and ω_2

end

return θ , ω_1 and ω_2

4. Scale Recovery with Estimated Depth

The initial egomotion \mathbf{T}_t^{t-1} can be obtained by minimizing the reprojection error from matched ORB features[20].

However, the obtained egomotion is not in real scale. This will cause the scale drift for the monocular visual odometry system. In this section, we introduce our scale recovery method using depth map predicted from section 3.

The observed point position relative to current camera coordinates is denoted by $\mathbf{p} = (x_i^c, y_i^c, z_i^c)^T \in \mathbb{R}^3$. The scale parameter α can be obtained by solving

$$z_i^{c'} \begin{pmatrix} u_i \\ v_i \\ 1 \end{pmatrix} = \alpha \begin{pmatrix} f_x & 0 & c_x \\ 0 & f_y & c_y \\ 0 & 0 & 1 \end{pmatrix} \begin{pmatrix} x_i^c \\ y_i^c \\ z_i^c \end{pmatrix} \forall i = 1, 2, \dots, n \quad (19)$$

where $z_i^{c'}$ is the estimated depth value in pixel $\mathbf{u}_i(u_i, v_i)$. We denote $\mathbf{Z}(u_i, v_i) = z_i^{c'}$. The estimated depth value for each point can be express as:

$$z_i^{c'} = \mathbf{Z} \left(\frac{x_i^c}{z_i^c} f_x + c_x, \frac{y_i^c}{z_i^c} f_y + c_y \right) \quad (20)$$

and the scale parameter is defined as:

$$\alpha = \frac{z_i^{c'}}{z_i^c} \quad (21)$$

Therefore, the residual of the i -th observed map point can be written as:

$$r_i = z_i^{c'} - \alpha z_i^c. \quad (22)$$

Ideally, the residual would be zero. On account of the noise introduced by the estimated depth and the noise is independent and identically distributed (IID), the distribution of r_i denotes $p(r_i)$. Because we use the matched feature points to calculate the scale. The number of points left is small. Taking small sample size and existence of outliers into consideration, the non-standardized student's t-distribution is adopted to model this distribution, which is capable of modeling the data with outliers. Then the scale recovery problem can be represented as a maximum likelihood estimation:

$$\alpha = \underset{\alpha}{\operatorname{argmax}} \prod_i^n p(r_i) \quad (23)$$

where

$$p(r_i) \propto \frac{1}{\sigma} \left(1 + \frac{1}{v} \left(\frac{r_i}{\sigma} \right)^2 \right)^{-\frac{v+1}{2}} \quad (24)$$

where σ and v are the scaling parameter and degree of freedom of student's t-distribution; α is the scale parameter to recover.

The maximum likelihood estimation can be solved by expectation maximization (EM) algorithm via calculating α and σ [13, 14] iteratively. Then we can obtain the transformation matrix with the scale α as

$$\mathbf{T}_t^{t-1} = \begin{pmatrix} \mathbf{R}_t^{t-1} & \alpha \mathbf{t}_t^{t-1} \\ \mathbf{0} & 1 \end{pmatrix} \quad (25)$$

Once the egomotion with absolute scale is calculated, the depth image \mathbf{Y} can be refined by Eq. 18. Because feature points normally do not locate in the near distance, we do not consider the appearance kernel term in scale recovery process. So ω_1 is set to zero. In this way, we can also speed up calculation. The egomotion can also be refined with the more accurate depth map. As a result, the egomotion and the depth map are becoming more and more accurate simultaneously. In our experiment, we only iterate this process once. Algorithm 2 describes the process of our visual odometry system.

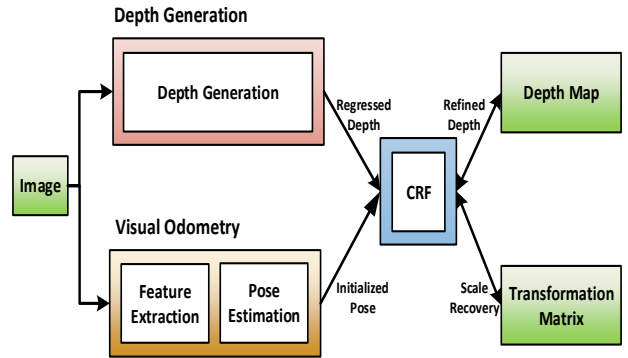


Figure 3. Structure of our system. There are two main threads, depth estimation and visual odometry threads. The depth estimation thread generates the depth map of the current frame. The visual odometry thread predicts the egomotion of the robot. Different depth maps are refined considering the time consumption. Sparse depth map is refined for visual odometry, and dense depth maps are refined for environment reconstruction.

5. Experiments

In this section, we conduct experiments to verify the effectiveness of our method on the KITTI dataset [8] for depth perdition and monocular visual odometry tasks. The KITTI dataset consists of image sequences from a driving vehicle with depth captured by a LiDAR and ground truth position by a GPS localization system. Figure 1 shows partial 3D reconstruction result of our method using egomotion and depth estimated by our method.

Our neural networks are trained and deployed on a NVIDIA TITAN X GPU with 12 GB memory. The deep residual part of our networks is ResNet-50 downloaded from model zoo. We apply the first 500 and first 1600 images in sequence 00 and 02 as training set. We first pre-train the neural networks with the ground truth depth without the CRFs layer. After the pre-training stage, we add the CRFs layer and fine tune the whole networks. Our networks are trained in an end-to-end fashion.

The depth is preprocessed by normalizing with $\frac{\log(x) - \min(\log(x))}{\max(\log(x)) - \min(\log(x))}$ [3, 18]. By doing this, the distri-

Algorithm 2: Scale recovery using depth predicted from image

Input: Given the image sequence $\{\mathbf{X}_t\}_{t=1}^n$, corresponding regressed depth images $\{\mathbf{Z}_t\}_{t=1}^n$ and camera parameters.

Initialize: $\alpha = 1$, \mathbf{T}_1 is the camera pose relative to the robot coordinate.

Output: The camera poses $\{\mathbf{T}_t\}_{t=1}^n$ and the optimized sparse depth images $\{\mathbf{Y}_t\}_{t=1}^n$

for $t = 2$ **to** n **do**

// Calculate the transformation matrix
 Extract and match feature points
 Minimize the reprojection error to calculate transformation matrix $\mathbf{T}_t^{t-1} = \begin{pmatrix} \mathbf{R}_t^{t-1} & \mathbf{t}_t^{t-1} \\ \mathbf{0} & 1 \end{pmatrix}$

// Scale parameter calculation
 Obtain k map points $\{\mathbf{p}_i\}_{i=1}^k, \mathbf{p}_i \in \mathbb{R}^3$
while $i < \text{maxIteration}$ **do**
 Calculate the corresponding depth $\{z_i^{c'}\}_{i=1}^k, z_i^{c'} \in \mathbb{R}$
 Get the scale parameter α using maximum likelihood estimation from Eq. (23)
 Update $\mathbf{T}_t^{t-1} = \begin{pmatrix} \mathbf{R}_t^{t-1} & \alpha \mathbf{t}_t^{t-1} \\ \mathbf{0} & 1 \end{pmatrix}$
 Optimize the depth image $\hat{\mathbf{Y}}_t$ from Eq. (18)
end
 Set $\mathbf{Y}_t = \hat{\mathbf{Y}}_t$
 Get current pose $\mathbf{T}_t = \mathbf{T}_t^{t-1} \mathbf{T}_{t-1}$
end

return $\{\mathbf{T}_t\}_{t=1}^n, \{\mathbf{Y}_t\}_{t=1}^n$

bution of depth is similar to a Gaussian distribution.

Unlike the depth prediction methods proposed in [17, 18], we do not apply super pixels in our framework. ORB features are applied in our method. Because ORB features are sparse in images, potential function in the same image is not involved in our depth refining process in visual odometry thread. This can accelerate the calculation of our program.

Figure 3 shows that the structure of our system contains two threads: depth generation thread and visual odometry thread. The depth generation thread provides regressed depth values to visual odometry thread. Egomotion obtained from visual odometry thread is passed to depth generation thread to get the refined depth. In order to accelerate the depth refining process in visual odometry subsystem, only depths of sparse feature points are refined. After obtaining the robot motion, the dense depth map can be obtained later or in a different thread.

Table 1. Evaluation on the KITTI dataset for depth estimation

Method	rel	log ₁₀	rms
Depth Transfer [12] (from [21])	0.171	0.076	2.830
Ranftl et al. (from [21])	0.148	0.065	2.408
Regressed depth with our method	0.162	0.062	2.571
Refined depth with our method	0.112	0.046	2.047

5.1. Depth estimation

The example images for qualitative evaluations are shown in Figure 4. The test images, ground truth depth map, regressed depth map and refined depth map are shown in Figure 4 (a), (b), (c) and (d), respectively. Only nearly 5% of image pixels have the ground truth depth values. We apply the inpainting method [16] for visualization. The refined results show that our algorithm can also remove the outliers to improve the accuracy of depth prediction. The accuracy of depth estimation has great impact on the performances of visual odometry. Applying the regression results directly without depth refining, the egomotion obtained by visual odometry will drift a lot.

The quantitative evaluation of depth estimation can be obtained with the following error metrics.

- average relative error (rel): $\frac{1}{N} \sum_{i=1}^N \frac{|d_i^{gt} - d_i|}{d_i^{gt}}$,
- average log₁₀ error (log₁₀): $\frac{1}{N} \sum_{i=1}^N |\log_{10} d_i^{gt} - \log_{10} d_i|$
- root mean squared error (rms): $\sqrt{\frac{1}{N} \sum_{i=1}^N (d_i^{gt} - d_i)^2}$

where d_i^{gt} and d_i are the ground truth and estimated depths indexed by i , and N is the total number of depths to evaluate.

We compare our method with other depth estimation approaches considering consecutive frames. In [12, 21], optical flow is applied to estimate the depths from videos. The test images of above methods are not provided in their paper. We evaluate our method on depth maps generated from over 11 thousand images from the sequence 00, 08, 09 and 10. According to their experiment settings, we also evaluate the generated depth within 20 meters. Outliers are not involved in the evaluation of refined results. The results are shown in Table 1. They indicate that our method can predict accurate depth map for inliers.

5.2. Monocular visual odometry

Our visual odometry method is evaluated on KITTI dataset [8] with the metrics provided by [8]. We compare

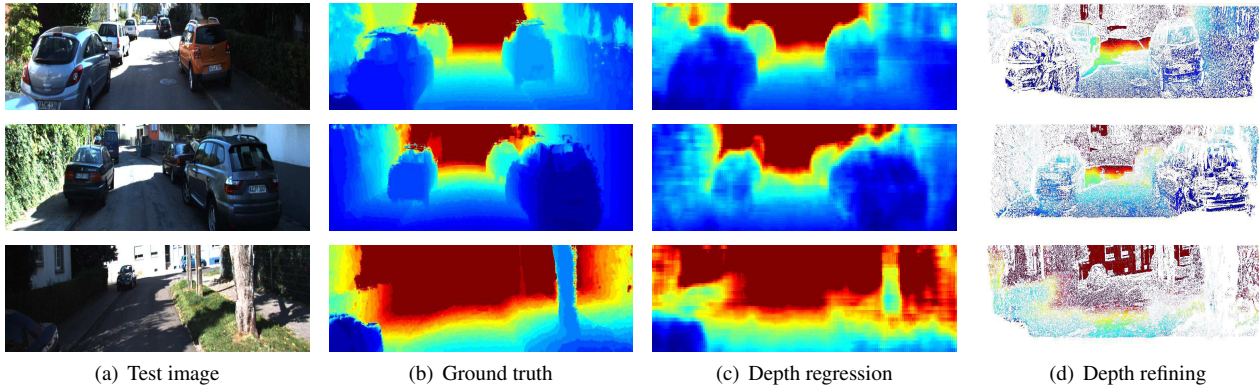


Figure 4. Examples of depth predictions results on three frames from the KITTI dataset. For each frame, we show (a) input color images, (b) ground truth depth (inpainted for visualization [16]), (c) results produced by depth regression, and (4) refined depth by our approach (red is far, and blue is close).

our result with other relevant visual odometry methods. Table 2 shows the translation and rotation errors in sequence 08, 09 and 10. Because the results of these sequences are reported and available for comparison [4, 24].

Our method gets a much better result than P-CNN VO [4] which is a recent method trying to regress the egomotion from optical flow using deep learning.

Comparing with Song’s and VISO2-M+GP’s results in translation [24], our method achieves a better performance in sequence 08 and 10. The reason why our method does not perform well in sequence 09 is that the scene is unstructured and contains many trees and bushes around the vehicle. This experiment illustrates that the accuracy of depth estimation is important for our scale recovery system. The regressed depths are not accurate enough if the environment lacks man-made references such as houses, vehicles. If we can train the networks with more data or applying different neural networks for different scenes, our method has potential to become more accurate and robust.

Figure 5 and 7 show the reconstructed trajectories and errors in translation and rotation of VISO-M (Monocular), VISO-S (Stereo) [9] and our method. Comparing with VISO-S, we obtain a comparative performance in translation on sequence 08 and 10. Figure 5(a) shows that our method is better than VISO-S for long distance driving. Apparently, our method is much better than VISO-M method. As for rotation estimation, our result is much better than other methods’. And our rotation calculation is based on that of ORB-SLAM method.

We also compare the performances of our method with ORB-M (Monocular) SLAM as shown in Figure 6. The scales are obtained by dividing the moving distances of consecutive frames to the ground truth. The expected value would be 1. Zero means track lost, which means it can not calculate the egomotion. From the results, we can find out that our method can keep the scale from drift for long dis-

tance motion (3000 meters in sequence 08). ORB-M can get a very good performance in calculating rotation. On the other hand, it is facing a large scale drift problem. Loop closure detection in ORB-SLAM can eliminate the scale drift. If the loop closure detection fail, it will not get a good performance for scale correction. Unlike the ORB slam method, we do not include the close loop detection and loop correction in our algorithm. Our method can also be a good compensation for other monocular odometry methods which are facing scale drift problem.

6. Conclusion

We present a novel scale recovery method for monocular visual odometry. The scale of translation is obtained using depth predicted from images, and depth is predicted with convolutional neural fields. The performance of depth prediction is improved by incorporating the consecutive frames and egomotion into our networks. The advantage of our method is that it can recover the scale and eliminate the scale drift from structural information of whole environments rather than from a fixed reference plane. Experiments are conducted on the KITTI dataset to verify the effectiveness of our method. The experimental results show that our algorithm can improve the accuracy on both visual odometry and depth estimation tasks.

Acknowledgements. We thank the anonymous reviewers for their valuable comments. This work is supported in part by the National Natural Science Foundation of China (61573260, 61673300), the Fundamental Research Funds for the Central Universities, the Basic Research Project of Shanghai Science and Technology Commission(16JC1401200, 16DZ1200903).

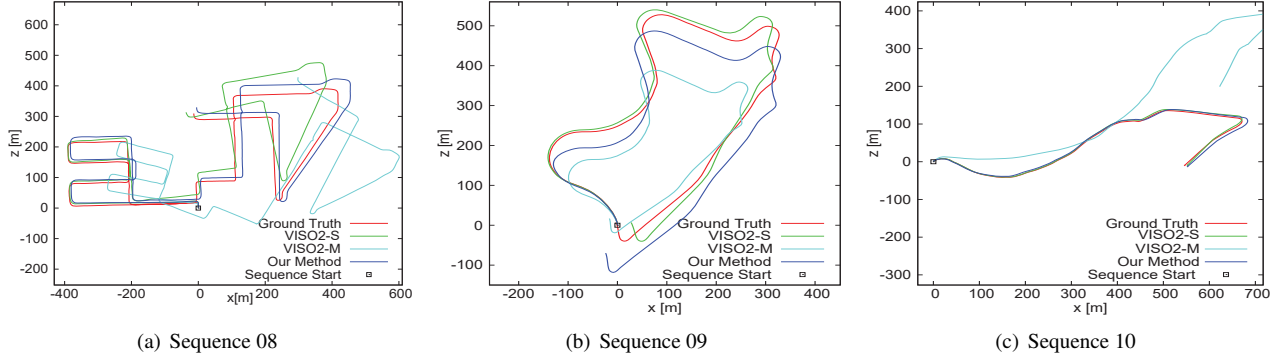


Figure 5. Reconstructed trajectories of sequences 08, 09, and 10 from the odometry benchmark of the KITTI dataset. We compare our method with VISO2-M (Monocular) and VISO2-S (Stereo).

Table 2. Comparison of translation and rotation errors for our method versus some monocular and stereo visual odometry methods on the KITTI benchmark.

Seq	VISO2-M (from [24])		VISO2-M+GP (from [24])		VISO2-Stereo (from [24])		P-CNN VO (from [4])		Song et al. (from [24])		Our Results	
	Trans (%)	Rot (deg/m)	Trans (%)	Rot (deg/m)	Trans (%)	Rot (deg/m)	Trans (%)	Rot (deg/m)	Trans (%)	Rot (deg/m)	Trans (%)	Rot (deg/m)
08	13.94	0.0203	6.64	0.0203	2.35	0.0104	7.6	0.0187	2.37	0.0044	2.22	0.0017
09	4.04	0.0143	3.04	0.0145	2.36	0.0094	6.75	0.0252	1.76	0.0047	4.14	0.0019
10	25.20	0.0388	21.3	0.0379	1.37	0.0086	21.23	0.0405	2.12	0.0085	1.70	0.0029
Avg	14.39	0.0245	10.33	0.0242	2.02	0.0095	8.96	0.00235	2.08	0.0059	2.68	0.0022

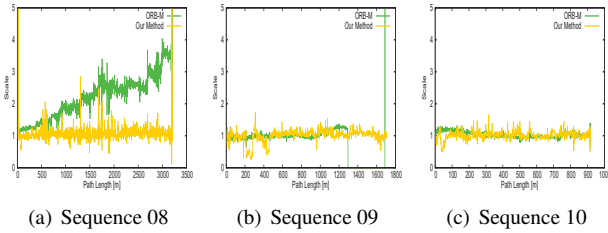


Figure 6. Scale recovery results in sequences 08, 09, and 10 from the odometry benchmark of the KITTI dataset. We compare our method with ORB-M (Monocular). ORB-M tracks lost on about 1300 m in sequence 09.

References

- [1] C. Cadena, L. Carlone, H. Carrillo, Y. Latif, D. Scaramuzza, J. Neira, I. D. Reid, and J. J. Leonard. Past, present, and future of simultaneous localization and mapping: Towards the robust-perception age. 2016.
- [2] S. Choi, J. H. Joung, W. Yu, and J. I. Cho. What does ground tell us? monocular visual odometry under planar motion constraint. In *International Conference on Control Automation and Systems*, pages 1480–1485, Oct 2011.
- [3] J. Civera, A. J. Davison, and J. M. Montiel. Inverse depth parametrization for monocular slam. *IEEE*

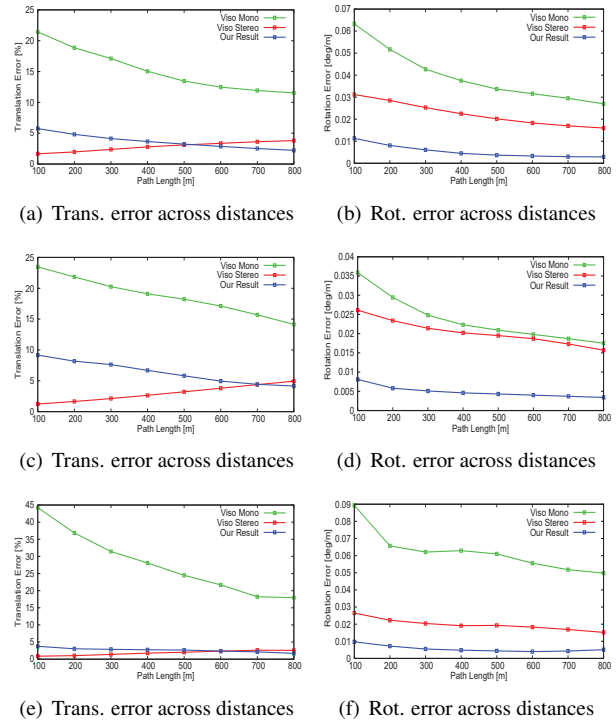


Figure 7. Visual odometry results on the KITTI benchmark, for rotation and translation errors over various distances.

- transactions on robotics*, 24(5):932–945, 2008.
- [4] G. Costante, M. Mancini, P. Valigi, and T. A. Ciarfuglia. Exploring representation learning with cnns for frame-to-frame ego-motion estimation. *IEEE Robotics and Automation Letters*, 1(1):18–25, 2016.
 - [5] T. Dang, C. Hoffmann, and C. Stiller. Continuous stereo self-calibration by camera parameter tracking. *IEEE Transactions on Image Processing*, 18(7):1536–1550, 2009.
 - [6] D. Eigen and R. Fergus. Predicting depth, surface normals and semantic labels with a common multi-scale convolutional architecture. In *Proceedings of the IEEE International Conference on Computer Vision*, pages 2650–2658, 2015.
 - [7] D. Eigen, C. Puhrsch, and R. Fergus. Depth map prediction from a single image using a multi-scale deep network. In *Proceedings of Advances in Neural Information Processing Systems*, pages 2366–2374, 2014.
 - [8] A. Geiger, P. Lenz, and R. Urtasun. Are we ready for autonomous driving? the kitti vision benchmark suite. In *Conference on Computer Vision and Pattern Recognition*, 2012.
 - [9] A. Geiger, J. Ziegler, and C. Stiller. Stereoscan: Dense 3d reconstruction in real-time. In *Intelligent Vehicles Symposium*, 2011.
 - [10] K. He, X. Zhang, S. Ren, and J. Sun. Deep residual learning for image recognition. In *Computer Vision and Pattern Recognition*, pages 770–778, 2016.
 - [11] A. Hyvärinen. Estimation of non-normalized statistical models by score matching. *Journal of Machine Learning Research*, 6(Apr):695–709, 2005.
 - [12] K. Karsch, C. Liu, and S. B. Kang. Depth transfer: Depth extraction from video using non-parametric sampling. *IEEE transactions on pattern analysis and machine intelligence*, 36(11):2144–2158, 2014.
 - [13] C. Kerl, J. Sturm, and D. Cremers. Robust odometry estimation for rgb-d cameras. In *IEEE International Conference on Robotics and Automation*, pages 3748–3754. IEEE, 2013.
 - [14] K. L. Lange, R. J. Little, and J. M. Taylor. Robust statistical modeling using the t distribution. *Journal of the American Statistical Association*, 84(408):881–896, 1989.
 - [15] B. Lee, K. Daniilidis, and D. D. Lee. Online self-supervised monocular visual odometry for ground vehicles. In *2015 IEEE International Conference on Robotics and Automation*, pages 5232–5238. IEEE, 2015.
 - [16] A. Levin, D. Lischinski, and Y. Weiss. Colorization using optimization. In *ACM Transactions on Graphics*, volume 23, pages 689–694. ACM, 2004.
 - [17] B. Li, C. Shen, Y. Dai, A. V. D. Hengel, and M. He. Depth and surface normal estimation from monocular images using regression on deep features and hierarchical crfs. pages 1119–1127, 2015.
 - [18] F. Liu, C. Shen, G. Lin, and I. Reid. Learning depth from single monocular images using deep convolutional neural fields. *IEEE Transactions on Pattern Analysis and Machine Intelligence*, 38(10):2024–2039, Oct 2016.
 - [19] J. Long, E. Shelhamer, and T. Darrell. Fully convolutional networks for semantic segmentation. In *IEEE Conference on Computer Vision and Pattern Recognition*, pages 3431–3440, 2015.
 - [20] R. Mur-Artal, J. M. M. Montiel, and J. D. Tardes. Orbslam: A versatile and accurate monocular slam system. *IEEE Transactions on Robotics*, 31(5):1147–1163, Oct 2015.
 - [21] R. Ranftl, V. Vineet, Q. Chen, and V. Koltun. Dense monocular depth estimation in complex dynamic scenes. 2016.
 - [22] A. Saxena, M. Sun, and A. Y. Ng. Make3d: learning 3d scene structure from a single still image. *IEEE Transactions on Pattern Analysis and Machine Intelligence*, 31(5):824–840, 2009.
 - [23] D. Scaramuzza and F. Fraundorfer. Visual odometry. *IEEE Robotics & Automation Magazine*, 18(4):80–92, 2011.
 - [24] S. Song, M. Chandraker, and C. C. Guest. High accuracy monocular sfm and scale correction for autonomous driving. *IEEE Transactions on Pattern Analysis and Machine Intelligence*, 38(4):730–743, April 2016.